

Myo9b is a key player in SLIT/ROBO-mediated lung tumor suppression

Ruirui Kong,¹ Fengshuang Yi,^{2,3} Pushuai Wen,¹ Jianghong Liu,¹ Xiaoping Chen,⁴ Jinqi Ren,² Xiaofei Li,⁵ Yulong Shang,⁶ Yongzhan Nie,⁶ Kaichun Wu,⁶ Daiming Fan,⁶ Li Zhu,¹ Wei Feng,² and Jane Y. Wu^{1,4}

¹State Key Laboratory of Brain and Cognitive Science and ²National Laboratory of Biomacromolecules, Institute of Biophysics, Chinese Academy of Sciences, Beijing, China.

³University of Chinese Academy of Sciences, Beijing, China. ⁴Department of Neurology, Center for Genetic Medicine, Lurie Cancer Center, Northwestern University Feinberg School of Medicine, Chicago, Illinois, USA. ⁵Department of Thoracic Surgery, Tangdu Hospital, and ⁶State Key Laboratory of Cancer Biology and Xijing Hospital of Digestive Diseases, Fourth Military Medical University, Shaanxi, China.

Emerging evidence indicates that the neuronal guidance molecule SLIT plays a role in tumor suppression, as SLIT-encoding genes are inactivated in several types of cancer, including lung cancer; however, it is not clear how SLIT functions in lung cancer. Here, our data show that SLIT inhibits cancer cell migration by activating RhoA and that myosin 9b (Myo9b) is a ROBO-interacting protein that suppresses RhoA activity in lung cancer cells. Structural analyses revealed that the RhoGAP domain of Myo9b contains a unique patch that specifically recognizes RhoA. We also determined that the ROBO intracellular domain interacts with the Myo9b RhoGAP domain and inhibits its activity; therefore, SLIT-dependent activation of RhoA is mediated by ROBO inhibition of Myo9b. In a murine model, compared with control lung cancer cells, SLIT-expressing cells had a decreased capacity for tumor formation and lung metastasis. Evaluation of human lung cancer and adjacent nontumor tissues revealed that Myo9b is upregulated in the cancer tissue. Moreover, elevated Myo9b expression was associated with lung cancer progression and poor prognosis. Together, our data identify Myo9b as a key player in lung cancer and as a ROBO-interacting protein in what is, to the best of our knowledge, a newly defined SLIT/ROBO/Myo9b/RhoA signaling pathway that restricts lung cancer progression and metastasis. Additionally, our work suggests that targeting the SLIT/ROBO/Myo9b/RhoA pathway has potential as a diagnostic and therapeutic strategy for lung cancer.

Introduction

As one of the most aggressive and highly metastatic malignancies, lung cancer ranks first in cancer-related deaths worldwide (1, 2). Metastasis is the leading cause of death among cancer patients (3, 4). Tumor cell invasion and migration are critical aspects in cancer metastasis. However, the endogenous mechanisms that suppress cancer invasion and metastasis remain to be elucidated.

The neuronal guidance cue SLIT comprises a family of secreted glycoproteins that were originally discovered to regulate axonal guidance and neuronal migration by binding to roundabout (ROBO) receptors (5–8). Subsequent studies demonstrated that SLIT/ROBO signaling also plays important roles outside of the nervous system, such as in the modulation of chemokine activation and migration of cells from multiple lineages (9–13). Recent studies suggest that the neuronal guidance molecule SLIT plays important roles in cancer (for recent reviews, see refs. 14–16). For instance, the *SLIT2* gene is inactivated in multiple types of cancers, including lung cancer, often as a result of promoter hypermethylation or loss of heterozygosity (LOH) (17–21). Nonetheless, the role of SLIT signaling in lung cancer and the underlying mechanisms are unclear.

To dissect the SLIT/ROBO signaling pathways, we searched for proteins interacting with the ROBO receptor and identified myosin 9b (Myo9b, also termed myosin IXb) as a ROBO-interacting protein. Myo9b is an unconventional myosin family motor protein that moves along actin filaments (22, 23). The vertebrate myosin IX family has 2 members: Myo9a and Myo9b. Myo9a is predominantly expressed in testis and brain (24), whereas Myo9b has been reported in the immune cells (25, 26). Different from other unconventional myosins, Myo9b contains a unique RhoGAP domain in its tail region in addition to the head (motor) domain with ATP- and actin-binding sites and the neck domain with 4 isoleucine-glutamine (IQ) motifs (27). Using this RhoGAP domain, Myo9b negatively regulates the small G protein RhoA, converting RhoA from the active GTP-bound form to the inactive GDP-bound form (25, 28, 29). The small G protein RhoA plays an important role in modulating the actin cytoskeleton during cell migration (e.g., refs. 30, 31, and references within). However, the structural basis for Myo9b function in regulating RhoA was unclear. The mechanisms by which the extracellular signals from guidance cues are transmitted to RhoA or other GTPases, thereby organizing coordinated changes in the actin cytoskeleton to promote directional cell migration, remain to be understood.

Here, we report that Myo9b is a previously unknown ROBO-interacting protein that mediates the SLIT inhibitory effect on lung cancer cell migration. We show that Myo9b specifically suppresses RhoA activation through its RhoGAP domain in lung cancer cells. Our x-ray crystallography data reveal that the Myo9b RhoGAP domain contains a unique patch that specifically recognizes RhoA. In lung can-

Authorship note: Ruirui Kong and Fengshuang Yi contributed equally to this work.

Conflict of interest: The authors have declared that no conflict of interest exists.

Submitted: February 26, 2015; **Accepted:** September 21, 2015.

Reference information: *J Clin Invest.* 2015;125(12):4407–4420. doi:10.1172/JCI81673.

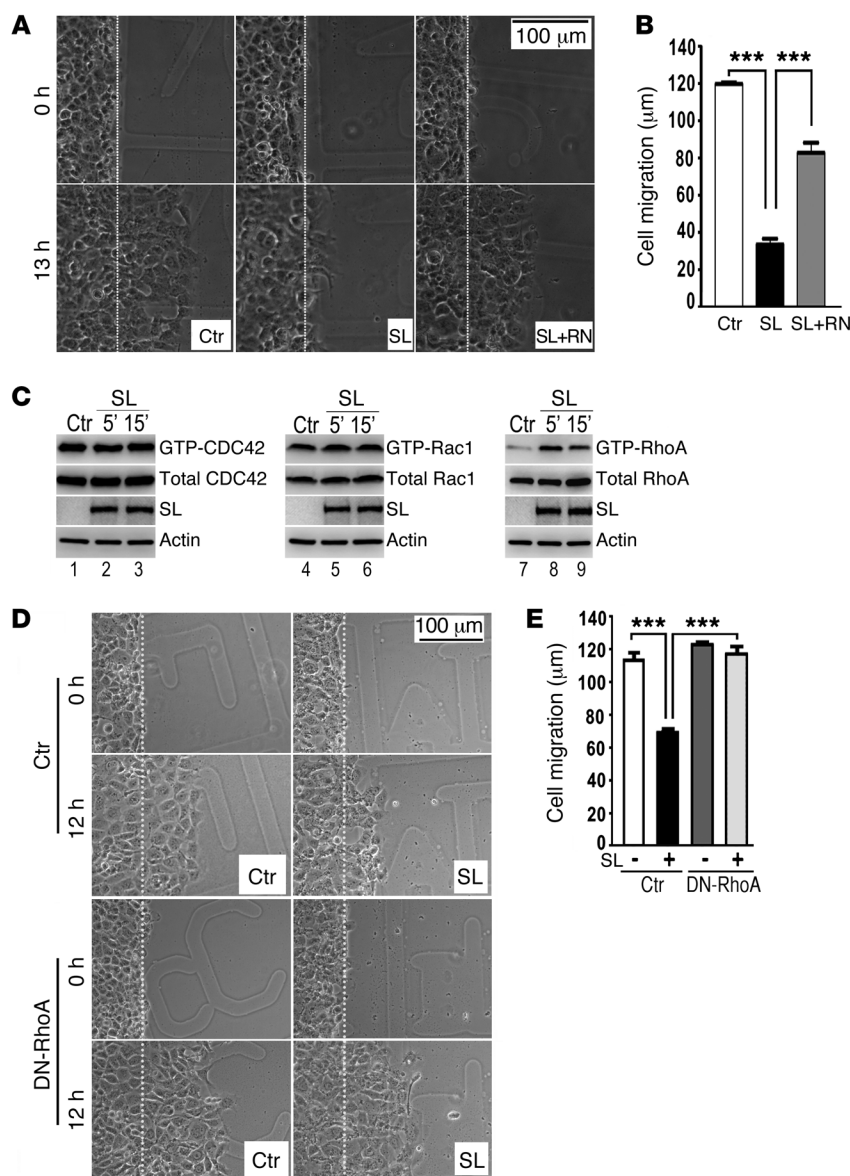


Figure 1. SLIT2 inhibits cell migration by regulating RhoA activity in lung cancer cells. (A) A wound-healing assay was performed using H1299 cells treated with control (Ctr), SLIT2 (SL), and ROBO1N (RN) media. At 0 and 13 hours after wound formation, phase-contrast images of migrating cells were obtained using an inverted microscope. Scale bar: 100 μ m. Data represent 5 independent experiments. (B) Quantification of cell migration distance over a 13-hour period. Data represent the mean \pm SEM of 3 independent experiments. *** P < 0.0001, Mann-Whitney U test. (C) H1299 cells were transfected with plasmids encoding either WT CDC42-Myc or Rac1-Myc and treated 48 hours after transfection with mock control or SLIT2 media for 5 or 15 minutes. Cell lysates were then prepared, a GST pull-down assay was performed using GST-PBD, and immunoblotting with anti-Myc Ab was done to measure active or total CDC42 or Rac1 levels in pull-down or total cell lysates, respectively. Active RhoA or total RhoA levels were measured by GST pull-down with GST-RBD and analyzed by immunoblotting with specific anti-RhoA Ab. SLIT protein levels in the culture media and actin (as an internal loading control) are also shown. (D and E) Cell migration in the H1299Ctr (Ctr) and H1299SLIT (SL) groups following transfection with a control vector or a Myc-tagged DN-RhoA plasmid as determined by wound-healing assay. Images were taken 0 and 12 hours after wound formation. Scale bar: 100 μ m. n = 5. Data in E represent the mean \pm SEM of 3 independent experiments. *** P < 0.0001, Mann-Whitney U test.

cer cells, the intracellular domain (ICD) of ROBO directly interacts with the Myo9b RhoGAP domain and inhibits its activity. Thus, our data demonstrate that the negative regulation of Myo9b by SLIT/ROBO signaling in lung cancer cells activates RhoA and inhibits cell migration. Supporting this model, our experiments showed that SLIT inhibits lung tumor invasion and metastasis in a xenograft mouse model. We found that Myo9b was highly expressed in human lung cancer tissues as compared with levels observed in the control samples. Consistently, increased Myo9b expression was associated with lymph node metastasis, advanced tumor stage, and poor patient survival. These results uncover what is, to our knowledge, a previously unknown SLIT/ROBO/Myo9b/RhoA signaling pathway that inhibits cell migration and suppresses lung cancer metastasis.

Results

SLIT2 inhibits cell migration by regulating RhoA activity in lung cancer cells. To investigate the involvement of SLIT/ROBO signaling in lung cancer pathogenesis, we first performed RT-PCR to exam-

ine the expression of *SLIT2* and its receptor *ROBO1* in various cell lines, including H1299 cells, derived from human lung cancer tissue. In most lung cancer cell lines surveyed and in a significant fraction of primary lung cancer samples examined, *SLIT2* expression was low or nondetectable (Supplemental Figure 1A; supplemental material available online with this article; doi:10.1172/JCI81673DS1). *ROBO1* protein, however, was detected in these lung cancer cell lines by Western blotting analysis using a specific anti-ROBO1 Ab (Supplemental Figure 1B).

To examine the effect of SLIT2 on lung cancer cell migration, we set up a wound-healing assay using H1299 lung cancer cells. The cells were treated with the mock control or SLIT2-containing media after wound formation. SLIT2 treatment significantly inhibited the migration of H1299 cells (Figure 1, A and B). To test the role of ROBO1 in mediating SLIT2 activity in lung cancer cells, we used ROBO1N, the soluble extracellular domain of ROBO1 capable of blocking SLIT signaling (6, 13, 32). Addition of ROBO1N to the wound-healing assay effec-

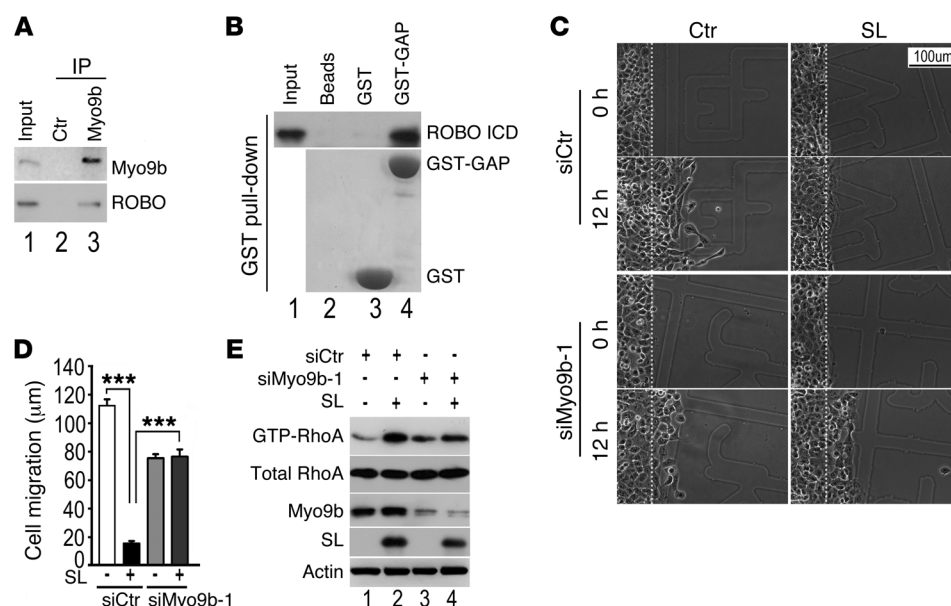


Figure 2. Myo9b is a key player in SLIT/ROBO signaling in lung cancer cells. (A) Interaction of endogenous ROBO1 and Myo9b proteins in H1299 lung cancer cells as demonstrated by co-IP experiments. IP was performed using the control IgG (Ctr) or anti-Myo9b Ab, followed by Western blotting. ROBO1 protein was detected in proteins immunoprecipitated by the specific anti-Myo9b, but not by the control Ab. (B) Interaction of the purified Myo9b RhoGAP domain (GST-GAP) with ROBO-ICD proteins as shown by GST pull-down experiments. (C) H1299Ctr and H1299SLIT (stably expressing SLIT2) cells transfected with siRNA against Myo9b (siMyo9b-1) or control siRNA (siCtrl) were examined for cell migration using a wound-healing assay. Representative images at 0 and 12 hours after wound formation. Scale bar: 100 μm. (D) Cell migration distance (μm) for the different treatment groups shown in C was quantified and is presented as the mean ± SEM. *** $P < 0.0001$, Mann-Whitney U test. Data are representative of 5 independent experiments. (E) H1299 cells stably expressing SLIT2 were transfected with siMyo9b-1 or siCtrl. GST pull-down experiments and Western blotting were performed to measure active and total RhoA levels.

tively reversed the inhibitory effect of SLIT2 on lung cancer cell migration (Figure 1, A and B), indicating that SLIT2 inhibits H1299 cell migration in a ROBO1-dependent manner. We also tested SLIT2 activity in another human lung cancer cell line, A549, and found that SLIT2 suppressed the migration of A549 cells as well and that ROBO1N abolished the SLIT2 inhibitory effect (Supplemental Figure 1, C and D).

To understand the molecular mechanism underlying SLIT2 function in lung cancer cells, we examined the signal transduction pathways involved. Our previous study indicated that SLIT reduces active CDC42 levels in neurons and that SLIT/ROBO GAP1 (srGAP1) is required for SLIT-induced suppression of CDC42 activity in neuronal migration (33). We therefore asked whether the srGAP1/Cdc42 pathway, observed in neurons, mediated the SLIT inhibitory effect on lung cancer cell migration. We systematically examined the effect of SLIT2 on small GTPases including CDC42, Rac1, and RhoA. H1299 cells expressing Myc-tagged CDC42 or Rac1 were treated with control or SLIT2 for 5 minutes or 15 minutes. Cell lysates were then incubated with GST-Pak-binding domain (GST-PBD), a protein domain specifically interacting with active (GTP-bound) CDC42 or Rac1 (30). Extracts from H1299 cells treated with control or SLIT2 for 5 minutes or 15 minutes were incubated with a GST-rhotekin-binding domain (GST-RBD), which selectively binds to the active form of RhoA (34). GTPases were detected in H1299 cell lysates by immunoblotting with corresponding Abs following the GST pull-down experiment. To our surprise, SLIT2 treatment did not affect active levels of either CDC42 or Rac1 (Figure 1C, lanes 1–3 and lanes 4–6, respectively). In contrast, SLIT2 treatment remarkably increased active RhoA levels

(Figure 1C, lanes 7–9), indicating that SLIT2 specifically modulates RhoA activity in lung cancer cells. We also used another method to examine SLIT2 activity in H1299 cells. Instead of adding SLIT2 to the culture media, we created 2 stable H1299 cell lines that over-expressed the human *SLIT2* gene. We detected similar RhoA, but not CDC42 or Rac1, activation when SLIT was expressed in H1299 cells (Supplemental Figure 1E). The observation that SLIT2 activates RhoA, but not CDC42 or Rac1, in lung cancer cells suggests that the mechanism by which SLIT2 regulates small GTPase activity in lung cancer cells is distinct from that in neurons.

To examine whether changes in RhoA activity were required for SLIT2 inhibition of lung cancer cell migration, we transfected H1299 control (H1299Ctr) and H1299 SLIT (H1299SLIT) cells with a dominant-negative form of RhoA (DN-RhoA) that was described previously (33). Wound-healing experiments were performed to determine the effect of RhoA on cell migration. Expression of the DN-RhoA mutant significantly reduced the inhibitory effect of SLIT2 on H1299 cell migration (Figure 1, D and E), indicating that SLIT2 inhibits lung cancer cell migration in a RhoA-dependent manner. These data show that SLIT2 inhibits cell migration by regulating RhoA activity in lung cancer cells.

Myo9b interacts with ROBO1 and mediates SLIT2-induced inhibition of cell migration and activation of RhoA. To dissect the SLIT/ROBO signaling pathways, we have been searching for proteins that interact with the ICD of the ROBO1 protein (32, 33). We performed yeast 2-hybrid screens, which identified one group of cDNA clones that encode the Myo9b protein, in addition to previously reported genes including srGAPs (33) and USP33 (32). RT-PCR and Western blotting experiments showed that Myo9b

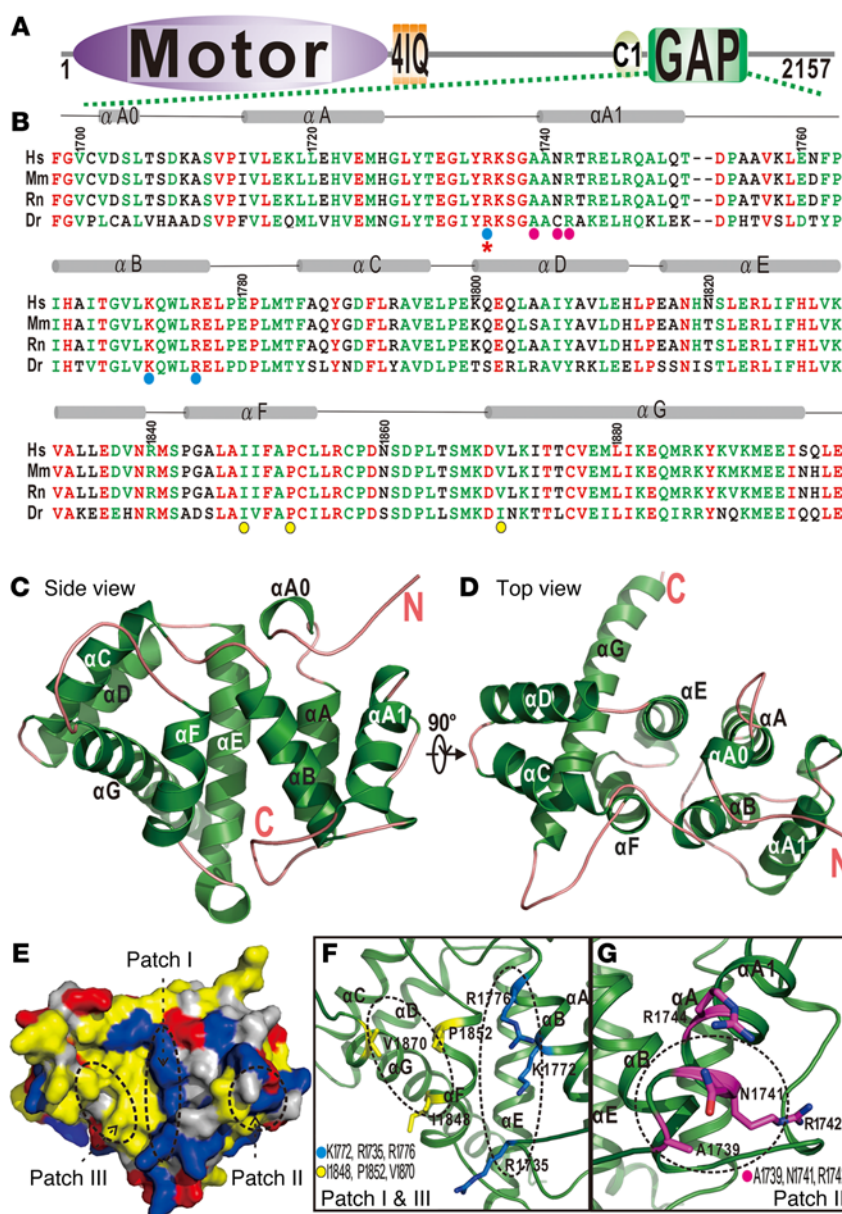


Figure 3. Overall structure of the Myo9b RhoGAP domain. (A) Domain organization of the Myo9b protein. (B) Structure-based sequence alignment of the Myo9b RhoGAP domains from different species: *Homo sapiens* (Hs) (NM_004145.3), *Mus musculus* (Mm) (NM_001142323.1), *Rattus norvegicus* (Rn) (NM_001271066.1), and *Danio rerio* (Dr) (XM_005171334.2). The identical and highly conserved amino acid residues are colored in red and green, respectively. Residue numbers of the Myo9b RhoGAP domain and the secondary structures are marked on the top. Residues involved in the formation of patches I, II, and III are highlighted with blue, magenta, and yellow dots, respectively, at the bottom of the rows. The active arginine finger of the RhoGAP domain is indicated by a red asterisk. (C and D) Ribbon diagrams of the crystal structure of the Myo9b RhoGAP domain from the side view (C) or top view (D). The α helical secondary structures (A0 to G) are labeled according to the canonical RhoGAP domain structure, with both N- and C-termini marked. (E) Surface representation of the Myo9b RhoGAP domain. In this diagram, the hydrophobic, positively charged, negatively charged residues, and remaining residues are shown in yellow, blue, red, and white, respectively. The Myo9b RhoGAP domain contains 3 patches (I–III) in the potential RhoA-binding site, similar to those in the p50RhoGAP protein. (F and G) Combined ribbon-stick model illustrating detailed features of the 3 patches. The side chains of the residues involved in the formation of patch I, patch III, and patch II are represented as sticks and are shown in blue, yellow, and magenta, respectively.

was expressed in lung cancer cell lines (Supplemental Figure 1, A and B), in contrast to a previous report that Myo9b expression was restricted to the immune system (25).

To confirm the interaction between ROBO1 and Myo9b in mammalian cells, we performed co-IP experiments using HEK293 cells transfected with plasmids encoding ROBO1 with an HA tag (HA-ROBO) or a vector control. Myo9b was detected in the immunoprecipitates formed with a specific anti-HA Ab from the HA-ROBO-expressing cells, but not from the control cells (Supplemental Figure 2A). To examine whether the endogenously expressed ROBO1 and Myo9b proteins were associated with each other in lung cancer cells, H1299 cell lysates were immunoprecipitated using anti-Myo9b or control IgG, followed by immunoblotting with anti-ROBO1. ROBO1 was detected in the proteins immunoprecipitated by anti-Myo9b Ab, but not by control IgG (Figure 2A). These results indicate that endogenous ROBO1 interacts with Myo9b in H1299 lung cancer cells.

ROBO1 is a transmembrane receptor containing 5 Ig domains, 3 fibronectin (Fn) III repeats in the extracellular region, and 4 conserved cytoplasmic (CC) motifs in the intracellular region (6). Myo9b contains a motor domain in the head region, 4 IQ motifs in the neck region, and a RhoGAP domain in the tail region (27). To characterize the ROBO1 and Myo9b domains involved in ROBO1-Myo9b interaction, we used a panel of ROBO1 deletion mutants (Supplemental Figure 2B and ref. 35) and constructed a series of Myo9b mutants (Supplemental Figure 2D). A co-IP assay was performed using lysates of H1299 cells that had been cotransfected with Flag-tagged Myo9b (Flag-Myo9b) and HA-tagged ROBO1 (the full-length or deletion mutants). All 4 CC motifs in the ICD of ROBO1 contributed to ROBO1-Myo9b interaction, whereas deletion of the ICD completely eliminated the interaction between ROBO1 and Myo9b (Supplemental Figure 2C). On the other hand, the RhoGAP domain in Myo9b is required for Myo9b association with ROBO1 (Supplemental Figure 2E). Therefore, Myo9b interacts with the ICD of ROBO1 via the RhoGAP domain.

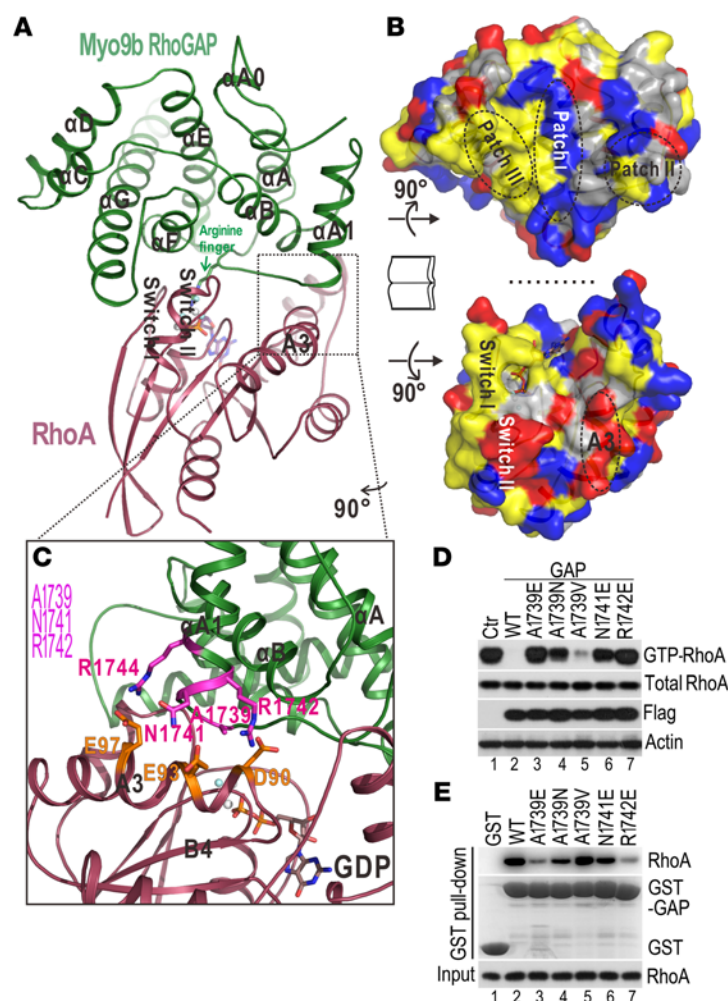


Figure 4. The Myo9b RhoGAP domain contains a unique region that specifically recognizes RhoA. (A) Ribbon diagram for the structural model of the Myo9b RhoGAP/RhoA complex. The Myo9b RhoGAP domain and RhoA are shown in green and red, respectively. The Myo9b RhoGAP domain interacts with RhoA through the 3 patches to form a stable complex. The switch I, switch II, and A3 helix of RhoA are responsible for the binding to the RhoGAP domain and are labeled. (B) "Open-book" view of the interaction interfaces between the Myo9b RhoGAP domain and RhoA by a surface representation. Here, the residues are colored as in Figure 3E. (C) Combined ribbon-stick model to illustrate in detail the interaction interface between patch II and the A3 helix. The side chains of the residues involved in the interface packing between patch II and the A3 helix are represented as sticks and are shown in magenta and orange, respectively. GDP and MgF_3 are shown as sticks and spheres, respectively. (D) Mutations inside patch II impaired Myo9b RhoGAP activity in the inactivation of RhoA. H1299 cells were transfected with the control vector (Ctr) or with plasmids encoding either the WT Myo9b RhoGAP domain (WT) or the indicated mutants. Cell extracts were subjected to GST pull-down assays to measure RhoA activity. (E) Mutations inside patch II disrupted binding between the Myo9b RhoGAP domain and RhoA. GST pull-down experiments were performed using recombinant WT or mutant forms of the GST-Myo9b RhoGAP domain and the cell lysates from HEK293 cells transfected with a Myc-RhoA plasmid.

We then asked whether Myo9b could directly interact with ROBO1. GST pull-down experiments were performed using the purified proteins GST-tagged Myo9b RhoGAP domain (GST-GAP) and maltose-binding protein-His6-tagged ROBO-ICD domain (MBP-His₆-ROBOICD) (see Supplemental Figure 2F for individual purified proteins). Following GST pull-down, the GST-GAP protein associated with MBP-His₆-ROBOICD was detected by Western blotting using anti-His Ab (Figure 2B), demonstrating that the purified Myo9b RhoGAP domain directly interacted with the ROBO-ICD domain. Consistently, the yeast 2-hybrid assay detected interaction between the ROBO-ICD and Myo9b (either GTPase-activating protein [GAP] alone or the protein kinase C conserved region 1 [C1] and RhoGAP domain [C1-GAP]) (Supplemental Figure 2G). These experiments indicate that the Myo9b RhoGAP domain can directly interact with the ICD of ROBO1.

Because Myo9b interacts with ROBO1 and displays RhoA-specific RhoGAP activity, we next tested whether Myo9b plays a role in mediating SLIT/ROBO signaling in the suppression of cell migration and the activation of RhoA in lung cancer cells. The wound-healing experiments were performed following knockdown of Myo9b expression using 2 independent Myo9b-specific siRNAs (siMyo9b) in H1299 cells. Immunoblotting experiments confirmed that siMyo9b efficiently reduced Myo9b

expression in H1299 cells (Figure 2E and Supplemental Figure 2J). Specific siRNAs against Myo9b, but not control siRNAs, abolished SLIT activity in inhibiting cell migration, indicating that the inhibitory effect of SLIT on lung cancer cell migration depends on Myo9b (Figure 2, C and D and Supplemental Figure 2, H and I). We observed no difference in cell proliferation between control and siMyo9b-mediated H1299 cells treated with SLIT2-containing media (Supplemental Figure 3, A and B). In addition, the GST pull-down experiments were performed using the GST-RBD to examine RhoA activation after H1299 cells were transfected with the control or with 2 Myo9b-specific siRNAs. When Myo9b was downregulated in H1299 cells, SLIT-induced RhoA activation was markedly reduced (Figure 2E and Supplemental Figure 2J), demonstrating that Myo9b is required for SLIT-induced RhoA activation in H1299 cells. Together, these data show that Myo9b is indeed important for SLIT/ROBO signaling in lung cancer cells.

Myo9b inactivates RhoA through its RhoGAP domain in lung cancer cells. Since Myo9b is critical for SLIT/ROBO signaling in the regulation of RhoA activity, we next tested whether Myo9b can specifically inactivate RhoA in lung cancer cells. We examined the effect of Myo9b on small GTPases, including RhoA, CDC42 and Rac1, in H1299 cells. Following transfection with the control or 2 Myo9b-specific siRNAs, H1299 cell lysates were

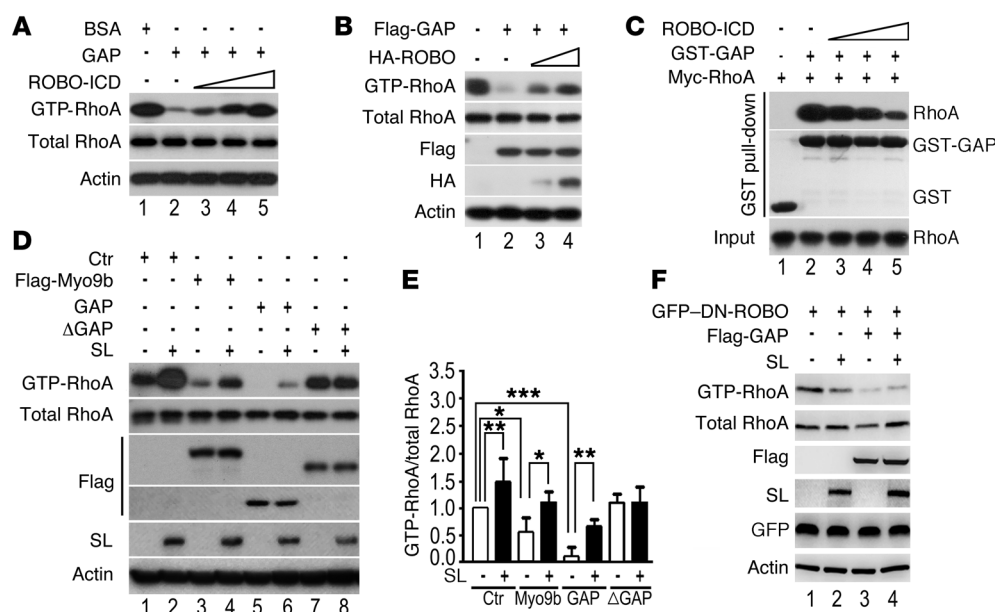


Figure 5. SLIT/ROBO signaling suppresses Myo9b RhoGAP activity. (A) Addition of purified ROBO-ICD suppressed Myo9b RhoGAP activity in a dose-dependent manner. Extracts from HEK293 cells transfected with a Myc-RhoA plasmid were incubated with different combinations of purified Myo9b-GAP or control (MBP only) or ROBO-ICD at a molar ratio of 1:1, 1:2, or 1:3. GTP-RhoA levels were measured by GST pull-down, coupled with Western blotting. (B) Expression of ROBO1 suppressed Myo9b RhoGAP activity. H1299 cells were cotransfected with Flag-tagged Myo9b GAP and HA-tagged ROBO1 at different doses. GTP-RhoA levels were measured as described in A. (C) Purified ROBO-ICD blocked Myo9b RhoGAP-RhoA interaction in a concentration-dependent manner. Lysates from HEK293 cells transfected with a Myc-RhoA plasmid were incubated with GST-GAP in the presence of different concentrations of ROBO-ICD protein. RhoGAP and RhoA interaction was examined using GST pull-down. (D) SLIT overexpression led to increased GTP-RhoA levels by suppressing Myo9b RhoGAP activity. The parental H1299 cell line or H1299 cells that stably expressed SLIT2 (shown as SL- or SL+, respectively, in the corresponding lanes) were transfected with the control vector or full-length Myo9b, or different Myo9b deletion mutants (Myo9bGAP or Myo9bΔGAP). Extracts were subjected to GST pull-down experiments, and immunoblot analyses of the pull-down products are shown. (E) GTP-RhoA levels were quantified and are shown as the mean \pm SEM of 3 independent experiments. * $P < 0.05$, ** $P < 0.001$, *** $P < 0.0001$, Mann-Whitney U test. (F) Expression of a dominant-negative mutant form of ROBO1 lacking its ICD (DN-ROBO) eliminated SLIT-induced activation of RhoA in H1299 cells. GST pull-down experiments, coupled with Western blotting, were performed to detect GTP-RhoA levels in H1299 cells following cotransfection with GFP-tagged DN-ROBO and Flag-tagged Myo9b-RhoGAP plasmids and treatment with the control or SLIT media.

prepared and incubated with GST-RBD or GST-PBD, respectively. The specific GTPase activity was determined by immunoblotting with corresponding Abs following the GST pull-down experiment. When Myo9b was downregulated, the levels of active RhoA and GTP-RhoA were dramatically increased, whereas the levels of either active CDC42 or active Rac1 were not affected (Supplemental Figure 4A). These data support the idea that Myo9b specifically inactivates RhoA in lung cancer cells. To examine whether the GAP activity of Myo9b depends on its RhoGAP domain, we performed a GST pull-down experiment using H1299 cells following transfection with plasmids expressing either the WT or deletion mutant Myo9b as Flag-tagged proteins, or the vector control. As expected, full-length Myo9b, C1-GAP, or the RhoGAP domain of Myo9b reduced active RhoA levels, but not those of CDC42 or Rac1 (Supplemental Figure 4B). To further examine the effects of the Myo9b RhoGAP domain on small GTPase activity, we prepared highly purified Myo9b RhoGAP domain protein for the GST pull-down experiments. Extracts from HEK293T cells respectively transfected with Myc-RhoA, Myc-CDC42, or Myc-Rac1 were incubated with the purified RhoGAP domain at different concentrations. Then, we performed GST pull-down experiments with active levels of small GTPases detected by Western blotting.

Consistent with our present findings and with those of previous studies of Myo9b, the purified Myo9b RhoGAP domain protein inhibited RhoA in a dose-dependent manner without affecting CDC42 or Rac1 (Supplemental Figure 4C), indicating that the Myo9b RhoGAP domain specifically modulates RhoA activity.

Structural analyses of the RhoGAP domain in Myo9b. To examine the mechanism underlying the RhoA-specific RhoGAP activity of Myo9b, we crystallized the Myo9b RhoGAP domain and determined its structure at 2.2-Å resolution (Figure 3 and Supplemental Table 4). From the overall structure, the Myo9b RhoGAP domain adopts a canonical RhoGAP fold with 9 α helices (namely, α A0 to α G, according to the canonical RhoGAP domain structure) (Figure 3, B-D). Among these helices, α A, α B, α E, and α F are arranged as a 4-helix bundle, forming the core of the structure (Figure 3, C and D). This 4-helix bundle is capped by the shortest α A0 helix that is likely to complete the core structure. One side of the central 4-helix bundle (the α A/ α B side) immediately packs with α A1 (Figure 3, C and D), whereas at its opposite side (the α E/ α F side), α C and α D form a helical hairpin that protrudes from the 4-helix bundle core. Interestingly, the last helix, α G, exhibits an orientation perpendicular to the other helices (except for α A0) and crosses the deep cave formed between the α C/ α D helical hairpin and the central 4-helix bundle (Figure 3, C and D).

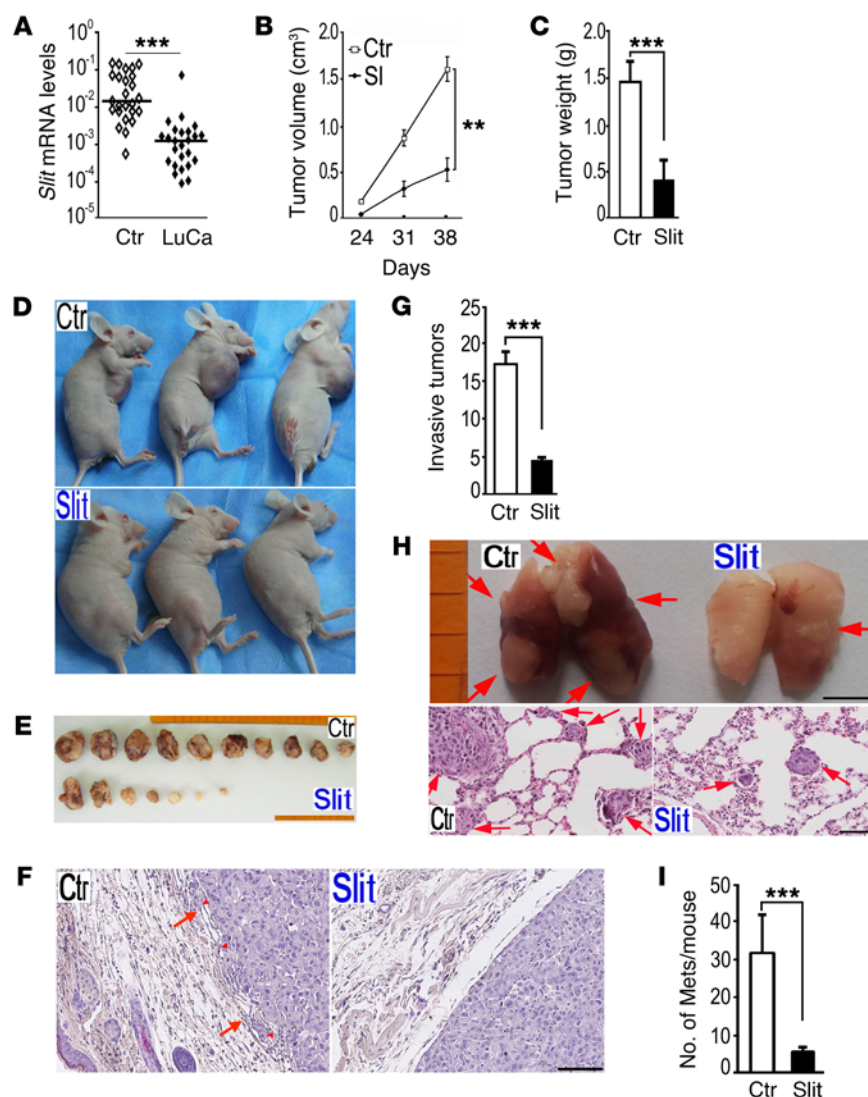


Figure 6. SLIT2 suppresses lung cancer invasion and metastasis. (A) SLIT2 mRNA levels were measured by quantitative RT-PCR in human lung cancer samples and paired adjacent noncancer control tissues. *** $P < 0.0001$, Student's t test. $n = 25$. LuCa, human lung cancer. (B) H1299Ctr and H1299SLIT cells were injected s.c. into nude mice. Tumor volume was monitored at different time points. *** $P < 0.001$, Mann-Whitney U test. $n = 10$. (C) On day 38 following tumor cell injection, mice were sacrificed and tumor weight measured. Differences in tumor size in the 2 groups were quantified. *** $P < 0.0001$, Mann-Whitney U test. (D) Images of representative mice from each group showing s.c. tumors. (E) Images of s.c. tumors in the corresponding groups. Scale bar: 10 mm. (F) Cross-sectional microscopic images of the s.c. tumors following H&E staining. Arrows indicate local invasive tumors with irregular borders and microcapillaries adjacent to invading tumor cells (marked by arrowheads) in H1299Ctr mice. Scale bar: 50 μ m. (G) Analyses of s.c. tumors in mice injected with H1299Ctr and H1299SLIT cells. The y axis shows the average number of invasive microfoci in the s.c. tumors. *** $P < 0.0001$, Mann-Whitney U test. (H) Morphology of lung metastases formed by H1299Ctr and H1299SLIT cells following s.c. implantation. Arrows indicate metastatic foci detected on the pulmonary surface. Scale bar: 1 mm (top), 50 μ m (bottom). (I) Numbers of lung metastatic foci (Mets) per mouse in the H1299Ctr and H1299SLIT groups. *** $P < 0.0001$, Mann-Whitney U test. Data are representative of 3 independent experiments.

The overall structure of the Myo9b RhoGAP domain is similar to that of the canonical RhoGAP domain of p50RhoGAP, especially in the central 4-helix bundle (Supplemental Figure 5). Consistent with this feature, the structure-based sequence alignment showed that the residues responsible for the 4-helix bundle formation are highly conserved among different members of the RhoGAP family (Supplemental Figure 5A). In contrast to the central 4-helix bundle, the neighboring α A1, α G, and α C/ α D helical hairpin showed some differences between the Myo9b RhoGAP and p50RhoGAP domains; e.g., the loop between α A1 and α B of the Myo9b RhoGAP domain is shorter than that of p50RhoGAP, whereas the last helix α G is relatively longer (Supplemental Figure 5, B–E). These structural differences may distinguish the Myo9b RhoGAP domain from RhoGAP domains in other proteins.

The Myo9b RhoGAP domain contains a unique patch that specifically recognizes RhoA. On the basis of the structure of the p50RhoGAP/RhoA complex (Supplemental Figure 6), the RhoA-binding site within the RhoGAP domain is formed by α A1, α B, α F, α G, and the α A/ α A1 and α F/ α G loops and can be divided into 3 patches (patches I, II, and III) with the active arginine finger located in the α A/ α A1 loop. Consistent with its structural similarity to the

p50RhoGAP domain (Supplemental Figure 6), the Myo9b RhoGAP domain contains a similar site with 3 patches that potentially form a binding surface to interact with RhoA (Figure 3, E–G). More specifically, patch I consists of R1735 from the α A1/ α B loop and K1772 and R1776 from α B (Figure 3, B and F); patch II is composed of A1739, N1741, R1742, and R1744 from the N-terminal half of α A1 (Figure 3, B and G); and patch III is formed by I1848 and P1852 from α F and V1870 from α G (Figure 3, B and F). Given that these patches formed a potential binding site (Figure 3E and Supplemental Figure 6), we confirmed by GST pull-down assay that the Myo9b RhoGAP domain indeed directly interacted with RhoA (Figure 4E).

The above-described similarity between the Myo9b RhoGAP and p50RhoGAP domains prompted us to build a structural model of the Myo9b RhoGAP/RhoA complex by replacing the RhoGAP domain in the p50RhoGAP RhoGAP/RhoA complex structure with the Myo9b RhoGAP domain. This model was further refined by molecular dynamics simulation in solution. As expected, the final structural model of the Myo9b RhoGAP/RhoA complex resembled that of the p50RhoGAP RhoGAP/RhoA complex, adopting a similar mode of interaction with 3 patches binding to RhoA (Figure 4, A and B, and Supplemental

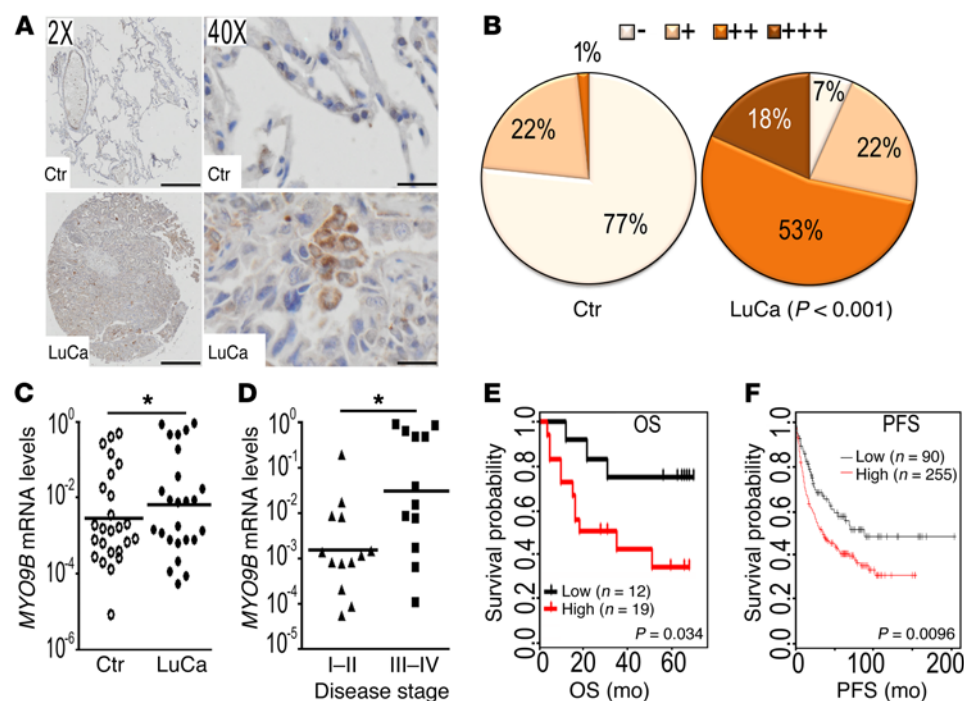


Figure 7. Myo9b expression and clinicopathological characteristics in lung cancer samples. (A) Immunostaining was performed to detect Myo9b protein in human lung cancer and matched adjacent noncancer control tissue samples. Representative images of Myo9b staining on tissue microarrays are shown at low ($\times 2$) and high ($\times 40$) magnification. Scale bars: 200 μm and 10 μm , respectively. $n = 60$. (B) Myo9b expression was scored by immunostaining signals. Myo9b expression levels (-, +, ++, +++) correspond to immunostaining scores of 0 to 3, respectively. $P < 0.001$, Pearson's χ^2 test. (C) *MYO9B* mRNA levels were higher in lung cancer samples as compared with the paired adjacent control tissues. The y axis shows *MYO9B* mRNA levels expressed as \log_{10} median-centered intensity. $*P < 0.05$, Student's t test. $n = 25$. (D) *MYO9B* mRNA levels in lung cancer samples at different stages (I–II and III–IV). $*P < 0.05$, Student's t test. $n = 13$ for the group with disease stages I–II; $n = 12$ for the group with disease stages III–IV. (E) Kaplan–Meier survival curves showing OS of lung cancer patients with Myo9b expression levels detected by immunostaining. Data are from 31 tissue samples for which survival information was available. $P = 0.034$, log-rank test. (F) Kaplan–Meier plots showing PFS of lung cancer patients stratified by lower-quartile expression of Myo9b in the caArray datasets. $P = 0.0096$, log-rank test.

Figure 6). Specifically, the positively charged patch I interacts with the negatively charged switch II, patch II packs with the A3 helix, and patch III forms extensive hydrophobic contacts with switch I. Because patches I and III of the RhoGAP domain are highly conserved, but patch II is diverse in different RhoGAP family proteins (Supplemental Figure 5A and Supplemental Figure 6), the specificity of the Myo9b RhoGAP domain toward RhoA may likely be determined by its patch II. Consistent with this feature, the structure-based sequence alignment of different Rho family proteins (RhoA, CDC42, and Rac1) shows that switch I and switch II, which are responsible for interacting with patch III and patch I of the RhoGAP domain, are also highly conserved (Supplemental Figure 7), whereas the sequences for the A3 helix, the corresponding site for binding to patch II, are diverse.

To further understand the specific recognition of RhoA by the Myo9b RhoGAP domain, we analyzed the interaction interface between patch II and the A3 helix. Patch II of the Myo9b RhoGAP domain is enriched in positively charged residues (R1742 and R1744) that form electrostatic interactions with negatively charged residues (D90 and E97) in the A3 helix of RhoA (Figure 4C). Moreover, N1741 in patch II is likely to interact with E93 in the A3 helix, and A1739 in patch II also forms hydrophobic interactions with the A3 helix (Figure 4C). In contrast, D90 is replaced by S88 in CDC42, and D90 and E97 are substituted with A88 and

A95, respectively, in Rac1. These amino acid residue substitutions make CDC42 and Rac1 poor candidates to interact with the Myo9b RhoGAP domain because of the positively charged residues within patch II of the Myo9b RhoGAP domain (Supplemental Figure 7). Consistent with these structure-based analyses, point mutations in patch II of the Myo9b RhoGAP domain to reverse its charged property, including A1739E, N1741E, and R1742E mutations, each remarkably decreased binding of the Myo9b RhoGAP domain to RhoA, thereby impairing the subsequent inactivation of RhoA (Figure 4, D and E). In contrast, the A1739V mutation did not affect Myo9b RhoGAP–RhoA interaction, whereas the A1739N mutation did (Figure 4, D and E), again, supporting an essential role of a hydrophobic interaction between A1739 of Myo9bGAP and the A3 helix of RhoA. Taken together, the Myo9b RhoGAP domain contains a unique positively charged patch II that specifically recognizes and inactivates RhoA.

Additionally, we substituted the corresponding amino acid residues in the A3 helix of CDC42 or Rac1 with those of RhoA for binding to patch II of RhoGAP, generating mutant forms of CDC42S88D/K94P or Rac1A88D/R94P/A95E. In a GST pull-down experiment, we demonstrated that the Myo9b RhoGAP domain inactivated these mutant forms of CDC42 and Rac1, but not the WT forms of CDC42 or Rac1 (Supplemental Figure 8, A and B). Consistent with this, the binding of Myo9b RhoGAP to

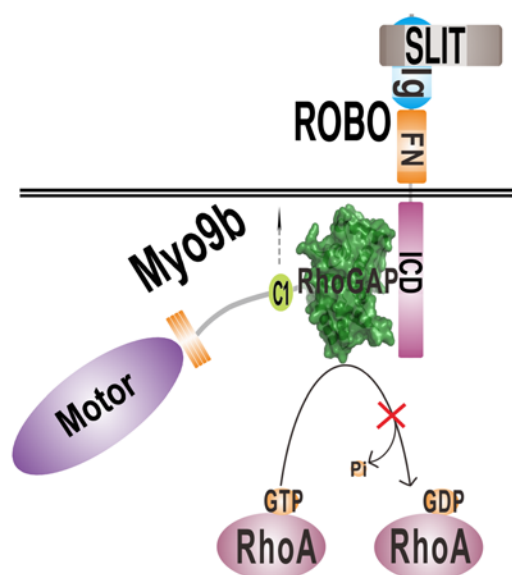


Figure 8. Working model depicting the SLIT/ROBO signal transduction pathway involving Myo9b and downstream RhoA. SLIT interacts with the transmembrane receptor ROBO to inhibit lung cancer cell migration in a ROBO-dependent manner. The ICD of ROBO (RPBP-ICD) binds to the RhoGAP domain of Myo9b and suppresses its GAP activity in converting GTP-RhoA to GDP-RhoA, leading to increased levels of GTP-RhoA and a subsequent suppression of cell invasion and migration. Pi, inorganic phosphate.

mutant forms of CDC42 or Rac1 dramatically increased as compared with the that seen in the WT form (Supplemental Figure 8, C and D), supporting the notion that the specific electrostatic interaction between patch II and the A3 helix may determine the specific recognition of RhoA by the Myo9b RhoGAP domain.

SLIT/ROBO signaling inactivates the Myo9b RhoGAP domain. Detection of the interaction between the ICD of ROBO1 and the Myo9b RhoGAP domain prompted us to investigate whether ROBO1 affected Myo9b RhoGAP domain activity. We performed a GST pull-down assay using GST-RBD and HEK293T cell lysates transfected with Myc-RhoA in the presence of various combinations of purified proteins: Myo9b RhoGAP and ROBO-ICD (as an MBP-tagged protein). The effect of ROBO-ICD on Myo9b RhoGAP activity was determined by Western blotting analysis of the pull-down products. Interestingly, Myo9b inhibitory effects on RhoA were suppressed by the addition of ROBO-ICD in a dose-dependent manner (Figure 5A, lanes 3–5), whereas addition of a control MBP-tagged protein alone showed no effect (Figure 5A, lane 2). Similarly, GST pull-down experiments using H1299 lung cancer cells that coexpressed a Flag-tagged Myo9b RhoGAP protein, together with different levels of full-length HA-tagged ROBO1 (HA-ROBO), demonstrated that ROBO1 suppressed Myo9b RhoGAP activity in RhoA inactivation (Figure 5B). Taken together, these results indicate that the ICD of ROBO suppresses Myo9b RhoGAP activity and prevents the conversion of GTP-RhoA to GDP-RhoA.

We next tested whether ROBO-ICD interfered with RhoGAP-RhoA interaction by performing GST pull-down experiments using purified ROBO-ICD protein and HEK293T cell lysates transfected with plasmids encoding Myc-tagged RhoA. These experiments showed that ROBO-ICD protein blocked the interaction of RhoGAP with RhoA in a concentration-dependent manner (Figure 5C), providing one mechanistic explanation for the inhibition of Myo9b RhoGAP activity by ROBO-ICD.

To further characterize the effect of SLIT2 on Myo9b RhoGAP activity in lung cancer cells, we performed GST-RBD pull-down experiments on a stable H1299 cell line that overexpressed SLIT2

following transfection with plasmids expressing either WT or mutant Myo9b as Flag-tagged proteins or the vector control. Myo9b activity in reducing active RhoA levels was suppressed by SLIT2, leading to increased levels of GTP-RhoA (Figure 5, D and E; compare lane 4 with lane 3 and lane 6 with lane 5, respectively). Interestingly, in the presence of a Myo9b mutant lacking its RhoGAP domain (Δ GAP), SLIT2 activity in increasing GTP-RhoA levels was blocked (Figure 5, D and E; compare lane 8 with lane 7), supporting the idea that SLIT2 activates RhoA by suppressing Myo9b activity in converting active GTP-RhoA to inactive GDP-RhoA and that the RhoGAP domain of Myo9b is required for SLIT2-induced RhoA activation.

We further tested whether SLIT2 inhibits Myo9b RhoGAP activity through the ROBO1 receptor. We coexpressed a ROBO1 mutant lacking its ICD as a GFP-tagged protein (GFP-DN-ROBO) and Flag-tagged Myo9b-GAP in H1299 cells. In these cells, SLIT2 treatment failed to induce RhoA activation, demonstrating that the inhibitory effect of SLIT2 on Myo9b-GAP activity is ROBO1 dependent (Figure 5F).

SLIT2 suppresses lung cancer invasion and metastasis. The data presented above allow us to define a SLIT/ROBO/Myo9b/RhoA signaling pathway that inhibits lung cancer cell migration in vitro. These data also suggest that SLIT2 is a suppressor for lung cancer. To investigate the role of SLIT2 in patients with lung cancer, we collected 25 pairs of lung tumor samples with the adjacent nontumor tissues. The expression of *SLIT2* mRNA was analyzed by real-time RT-PCR with *GAPDH* as an internal control. *SLIT2* expression was significantly decreased in lung tumors as compared with expression levels detected in the paired adjacent control tissues (Figure 6A). To survey data on more patients, we analyzed published datasets for *SLIT2* expression in lung cancer using the Oncomine database (www.oncomine.org) and gene microarray data analysis tools (36). Data from multiple datasets show that *SLIT2* gene expression is significantly downregulated in human lung cancer samples as compared with controls (Supplemental Figure 9A), consistent with the findings of a previous report involving a relatively small cohort (20). Kaplan-Meier analyses of different human lung cancer microarray datasets, including those found in the caArray database (www.kmplot.com) and in the NCBI's Gene Expression Omnibus (GEO) database (GEO GSE31210) (37), show that higher levels of *SLIT2* expression are associated with longer overall survival (OS) and progression-free survival (PFS) of patients (Supplemental Figure 9, B and D). Even among late-stage lung cancer patients with grade III tumors, lower *SLIT2* expression levels were associated with a shorter OS time (Supplemental Figure 9C). Importantly, in lung cancer patients with lymph node metastasis, higher *SLIT2* expression levels still correlated with a better prognosis of OS (Supplemental Figure 9C). Our analysis of 178 lung cancer samples from The Cancer Genome Atlas (TCGA) published dataset (38) demonstrates that approximately 8%, 7%, and 7% of

the human lung cancer cases showed genetic alterations (including homozygous deletion and mutations) in the *SLIT2*, *SLIT3*, or *ROBO1* genes, respectively (Supplemental Figure 9, E–G), suggesting that the *SLIT* or *ROBO1* gene plays an important role in lung cancer pathogenesis. Taken together, these data strongly support a role of *SLIT2* in suppressing lung cancer in humans.

To determine whether *SLIT2* could suppress lung cancer invasion and metastasis in vivo, we established a xenograft animal model using H1299 cells in which endogenous *SLIT2* expression levels were low. We prepared stable H1299 cell lines expressing human *SLIT2* (H1299SLIT) or the vector control (H1299Ctr) and examined their behavior in the animal model. We monitored tumor formation following s.c. injection of either H1299Ctr or H1299SLIT cells into nude mice. By day 24 after tumor cell injection, palpable tumors were detected. Animals were euthanized and examined for local tumor invasion and lung metastasis. In the H1299Ctr group, all 10 mice injected developed s.c. tumors, whereas in the H1299SLIT group, only 7 of 10 mice showed detectable s.c. tumors (Figure 6E). The average volume and weight of the primary tumors in the H1299Ctr group were significantly greater than those of the *SLIT2*-expressing tumors in the H1299SLIT group (Figure 6, B–D), demonstrating that *SLIT2* expression in H1299 cells suppresses tumor growth or invasion in vivo. Histological examination of these primary tumors revealed that the majority of H1299Ctr tumors exhibited local invasion, with irregular borders and numerous microcapillaries adjacent to invading tumor cells, whereas most tumors derived from H1299SLIT cells were surrounded by fibrous capsules with smooth, clear borders (Figure 6, F and G, and Supplemental Table 1). These findings indicate that *SLIT2* expression significantly reduced invasion by H1299 lung cancer cells in vivo. We performed further histological examination of mouse lung tissues to evaluate lung metastasis. In the H1299Ctr group, all mice showed lung metastasis, whereas only 3 of 10 mice in the H1299SLIT group showed lung metastasis (Figure 6H and Supplemental Table 2). In these mice, H1299SLIT cells induced much reduced lung metastasis as compared with the H1299Ctr cells, in terms of both the size and number of lung metastatic tumors (Figure 6, H and I, and Supplemental Table 2). These results demonstrate that *SLIT2* inhibits lung cancer invasion and metastasis in our mouse model, supporting the idea that *SLIT2* is a lung cancer-suppressor gene.

Myo9b is highly expressed in lung cancer, and high *Myo9b* expression levels are correlated with lung cancer progression. We investigated the potential involvement of *Myo9b* in human lung cancer. First, we examined *Myo9b* expression in a tissue-array panel containing 60 human lung cancer samples with corresponding matched adjacent nontumor tissues. Fifty-six of the sixty (93%) lung cancer tissue samples showed positive *Myo9b* immunostaining signals, whereas only 14 of 60 (23%) paratumor control tissue samples were *Myo9b* positive (Figure 7A for a representative tissue pair and Figure 7B). Consistent with our immunostaining data, real-time RT-PCR analyses of a separate cohort of 25 pairs of human lung cancer and control samples showed that *MYO9B* mRNA levels were significantly increased in the lung cancer samples as compared with the levels detected in the adjacent nontumor tissue controls (Figure 7C), further supporting the finding that *Myo9b* expression is upregulated in human lung cancer.

We further analyzed the lung cancer samples to determine whether there was a correlation between *Myo9b* expression and the clinicopathological features of lung cancer patients. We found no significant correlation between *Myo9b* expression and patients' age, sex, or tumor size. However, the majority of patients who had lymph node metastasis showed increased *Myo9b* expression (15 of 16 patients, Supplemental Table 3). Thus, *Myo9b* expression was correlated with lymph node metastasis, suggesting that *Myo9b* may promote lung cancer metastasis. In addition, 35 of 43 lung cancer patients with high *Myo9b* expression levels had an advanced pathological disease stage (Supplemental Table 3). Consistently, we found that *MYO9B* mRNA levels were higher in the more advanced-stage lung tumors (Figure 7D). Therefore, increased *Myo9b* expression is associated with lung cancer progression in patients.

We also examined the correlation between OS of patients and their *Myo9b* expression levels using the Kaplan-Meier method. Higher *Myo9b* expression levels were associated with a lower probability of OS (Figure 7E). Our analyses of the published lung cancer datasets (37) consistently showed that patients with higher levels of *Myo9b* expression had significantly shorter PFS than did those expressing lower levels of *Myo9b* (Figure 7F). These results support the notion that *Myo9b* functions as a tumor-promoting factor in lung cancer progression.

Discussion

Lung cancer is a leading cause of death and a major health problem in both developed and developing countries (39). Significant efforts have been made to understand the pathogenetic mechanisms underlying lung tumorigenesis (refs. 2–4, and references within). A number of tumor-promoting mutations have been found in *EGFR* and *KRAS* genes in patients with lung cancer. Lung cancer tumor-suppressor genes, including TP53, P16, LKB1/STK11, NF1, RASSF1, APC, BRG1, PTEN, and RB, which regulate cell cycle, cell proliferation, and cell death, have also been discovered (reviewed in refs. 40, 41). However, little is known about the endogenous mechanisms that suppress lung cancer invasion and metastasis.

In this study, we present both in vitro and in vivo evidence that supports an important role of *SLIT2* in the suppression of lung cancer. We show that *SLIT2* inhibited migration of lung cancer cells in a ROBO-dependent manner. This is consistent with our previous studies of breast cancer (32) and with other studies of cancers such as glioma (42) and medulloblastoma (43). In the xenograft mouse model used in the present study, we demonstrate that increased expression of *SLIT2* reduced tumor formation, local invasion, and lung metastasis.

The expression of *SLIT1* is restricted to the brain, whereas both *SLIT2* and *SLIT3* are highly expressed in brain and lung tissues (13, 44). Consistent with previous studies (18, 20), our analyses show that *SLIT2* is substantially downregulated in human lung cancer and that low *SLIT2* expression levels are associated with poor survival of lung cancer patients. It has been reported that in developing or postnatal mouse lung tissues, *SLIT2* is expressed in the mesenchymal compartment and larger airway epithelium, whereas *SLIT3* expression is detected in the endothelium of large vessels associated with conducting airways (44). It is possible that the human *SLIT2/3* genes expressed in lung tissue play a role in restricting lung cancer

invasion and metastasis. Interestingly, approximately 8% or 7% of patients with lung cancer showed genetic alterations in the *SLIT2* or *SLIT3* genes, respectively. In addition, mutations in the human *ROBO1* gene have been detected in approximately 7% of lung cancer cases (Supplemental Figure 9). Together, our results strongly support a role of SLIT/ROBO signaling in the suppression of lung cancer invasion and metastasis.

Myo9b is a RhoGAP protein that modulates lamellipodia protrusion and tail retraction by suppressing RhoA activation in migrating immune cells (25). To our knowledge, the involvement of Myo9b in cancer has not been reported previously. The data presented here indicate that Myo9b is a ROBO-interacting protein that is highly expressed in human lung cancer. The ICD of ROBO1 interacts with the Myo9b RhoGAP domain and suppresses Myo9b RhoGAP activity, as illustrated in our working model depicted in Figure 8. Thus, SLIT2/ROBO1 signaling suppresses Myo9b RhoGAP activity in the conversion of GTP-RhoA to GDP-RhoA, leading to increased GTP-RhoA. Our analyses of samples from patients show that increased expression of Myo9b correlates with advanced disease stage, lymph node metastasis, poor OS, and shortened PFS. Taken together, our study uncovers what is, to our knowledge, a previously unknown pathway, SLIT/ROBO/Myo9b/RhoA, that mediates SLIT/ROBO signaling in lung cancer cells.

Myo9b contains a RhoGAP domain at its carboxyl terminus (see Figure 3A) that has been reported to inactivate RhoA, but not CDC42 or Rac1 (45). However, the molecular mechanism underlying the specific GAP activity of this RhoGAP domain toward RhoA remained unclear. In this study, we have determined the structure of the Myo9b RhoGAP domain (Figure 3). In comparison with other RhoGAP domains, the Myo9b RhoGAP domain contains a unique positively charged patch II that can specifically recognize the negatively charged A3 helix of RhoA (Figure 4 and Supplemental Figure 5). Mutations in this patch II region decreased the binding of the Myo9b RhoGAP domain to RhoA and impaired the subsequent RhoA inactivation (Figure 4). Moreover, the corresponding interaction site in CDC42 or Rac1 for patch II is different from that in RhoA and would not be well recognized by the Myo9b RhoGAP domain (Supplemental Figure 7). Consistent with previous data (46), the specificity of the RhoGAP domain for Rho GTPases is most likely determined by the interaction between patch II and the A3 helix. Together, our data reveal a structural basis for the RhoA-specific GAP activity of the Myo9b RhoGAP domain. It is likely that the paradigm in which the unique positively charged patch II identified in the Myo9b RhoGAP domain specifically recognizes RhoA may also be extended to other proteins containing such RhoA-specific RhoGAP domains.

The Rho family of GTPases plays important roles in cell migration by modulating actin and microtubule dynamics, myosin activity, and cell-extracellular matrix and cell-cell interactions (30, 31, 47). The roles of RhoA in cancer cell invasion and migration are highly complex. RhoA is capable of mediating stress fiber formation and generating the contractile force needed for retraction of the trailing edge during cell migration (refs. 47, 48, and references within). RhoA was also reported to function in membrane ruffling and lamellae formation (49). However, the expression and function of RhoA in lung cancer remain unclear. Our data show that constitutively active RhoA inhibits migration

in lung cancer cells, indicating that activated RhoA suppresses lung cancer cell migration (Supplemental Figure 1, F and G). In our study, increased SLIT2 expression or SLIT2 treatment led to RhoA activation in lung cancer cells. Lung cancer cells expressing SLIT2 showed significantly reduced cell migration in vitro and decreased cancer invasion and metastasis in vivo. These findings led us to propose that SLIT2 activates RhoA signaling to inhibit lung cancer cell migration. A recent study shows that miR-194 suppresses non-small-cell lung cancer metastasis through activation of the RhoA pathway, producing enhanced development of actin stress fibers and impaired migration of cancer cells (50). Ablation of p120-catenin enhances invasion and metastasis of human lung cancer cells by inactivating RhoA (51), consistent with our results. Recent studies suggest that RhoA activity may have a tumor-suppressive role in diffuse gastric cancer and T cell lymphoma (52–58).

Our findings led us to propose a working model for the newly defined SLIT/ROBO/Myo9b/RhoA pathway in mediating the inhibitory effect of SLIT2 on lung cancer cell migration (Figure 8). In this model, SLIT2 acts to suppress lung cancer cell migration in a ROBO-dependent manner. The ICD of ROBO1 binds to the RhoGAP domain of Myo9b, resulting in the suppression of Myo9b RhoGAP activity and leading to increased levels of GTP-RhoA. These data, to our knowledge, uncover a previously unknown role of Myo9b in lung cancer.

It should be noted that studies from several groups, including our own, have shown that SLIT/ROBO signaling in neurons and in different types of cancers may use distinct signal transduction pathways. For example, the SLIT/ROBO/srGAP/CDC42 pathway seems to play a major role in neurons (e.g., see ref. 33), whereas USP33 is required for SLIT/ROBO signaling in commissural neurons and breast cancer cells (e.g., refs. 32, 35). Here, our data demonstrate an important role for the SLIT/ROBO/Myo9b/RhoA pathway in lung cancer. The observation that Myo9b expression is increased in multiple cohorts of lung cancer samples also suggests that Myo9b is a potential therapeutic target for lung cancer. It is conceivable that reducing or silencing Myo9b expression or blocking its activity in lung cancer cells may provide therapeutic benefits for patients with metastatic lung cancer who show increased Myo9b expression levels. Our study defines what is, to our knowledge, a previously unrecognized signal transduction pathway for SLIT in the suppression of lung cancer invasion and metastasis that involves ROBO/Myo9b/RhoA signaling. Future studies are necessary to understand the cross-communication of the SLIT/ROBO/Myo9b/RhoA pathway with other signal transduction pathways critical for the extremely complex process of lung cancer development and progression.

Methods

Crystallization, data collection, and structure determination. Crystallization of the Myo9b RhoGAP domain (15 mg/ml in 50 mM Tris-HCl, pH 8.0, 100 mM NaCl, 1 mM EDTA, 1 mM DTT) was achieved at 16°C using the vapor diffusion method (sitting drop) in 0.2 M NH_4Ac , 0.1 M Bis-Tris, pH 6.0, and 20% PEG 3350. Before being flash-frozen in liquid nitrogen, the crystal was cryoprotected with the mother liquor supplemented with 1 M LiAc. Diffraction data were collected at the beamline BL17U of the Shanghai Synchrotron Radiation Facility with a wavelength of 0.979 Å at 100 K. The dataset was processed

and scaled using iMOSFLM (59) and the SCALA module in the Computational Collaborative Program No. 4 (CCP4) software suite (60). The structure of the Myo9b RhoGAP domain was solved by the molecular replacement method using the p50RhoGAP RhoGAP domain (Protein Data Bank [PDB] code 1OW3) as a research model with PHASER (61). The structure model was further manually built with COOT (62) and refined with Phenix software (63). The overall quality of the final structural model of the Myo9b RhoGAP domain was assessed by PROCHECK (64). The protein structure figures were prepared using the PyMOL program (<http://www.pymol.org>). The statistics for the data collection and structural refinement are summarized in Supplemental Table 4. The coordinate of the crystal structure of the Myo9b RhoGAP domain is deposited in the PDB (accession number 5C5S).

Molecular dynamics simulations. The initial structural model of the Myo9b RhoGAP/RhoA complex was obtained by replacing the RhoGAP domain in the p50RhoGAP RhoGAP/RhoA complex structure (PDB code 1OW3) with the Myo9b RhoGAP domain. The model structure was then soaked in a $96 \times 96 \times 96 \text{ \AA}^3$ water box, which included 26 Mg^{2+} and 48 Cl^- to neutralize the system. The NAMD package (65) and the CHARMM22 all-atom force field (66) were used for energy minimization and molecular dynamics simulations. Under periodic boundary conditions, a 12- \AA cutoff was used for van der Waals interactions, and particle mesh Ewald summation was used to calculate the electrostatic interactions. Four independent simulations were performed. For each simulation, energy was first minimized in multiple steps to avoid any possible clashes. The energy-minimized system was then equilibrated for 10 ns, with the temperature controlled at 310 K by Langevin dynamics and the pressure controlled at 1 atm by the Langevin piston method. With the equilibrated structures, 50-ns free dynamics simulation was performed for each system. The simulation trajectories were analyzed with the Visual Molecular Dynamics (VMD) program (67).

Animal experiments. H1299Ctr and H1299SLIT cells were inoculated s.c. into the right flank (6×10^6 cells/mouse; $n = 10$) of 6-week-old female BALB/c nude mice as described previously (68). Tumor volumes (V) were measured every week and calculated using the equation $V(\text{mm}^3) = a \times b^2/2$, in which a was the largest dimension and b was the perpendicular diameter. Animals were euthanized when the largest primary tumor grew to approximately 1,000 mm^3 or the animal's condition deteriorated. Lung tumors and surrounding normal lung tissue were removed and dissected for histological examination. Tissues were fixed in 4% paraformaldehyde and embedded in paraffin. H&E staining and immunohistochemical analyses were performed on tissue sections as previously reported (42).

Tissue microarray and immunohistochemical staining. Deidentified lung tumor tissue samples were collected from 60 consented patients at Xijing Hospital (Xi'an, China) following institutional and national guidelines. The study cohort consisted of tumors and corresponding adjacent nontumor lung tissues from these same patients. Array blocks were sectioned to produce serial 4- μm sections for immunohistochemical staining. Tissue microarray sections were immunostained with the Myo9b Ab, the specificity of which was confirmed by antigen competition experiments (Supplemental Figure 10 and Supplemental Methods). Myo9b immunostaining signals are mostly in the cytoplasm of lung cancer cells that are positive for E-cadherin but not the mesenchymal cells (see Supplemental Figure 11).

Immunohistochemical analysis of human lung cancer tissues. IHC was performed on formalin-fixed, paraffin-embedded human lung cancer tissue sections. Polyclonal anti-Myo9b Ab (1:350) was used with HRP-conjugated goat anti-rabbit secondary Ab and DAB for color development. For a control, the samples were incubated with the preimmune rabbit IgG instead of the primary Ab. Myo9b immunostaining was scored from 0–3 according to the signal intensity and distribution (0, <5%; 1, 5%–25%; 2, 25%–50%, and 3, >50%). Cytoplasmic yellow granule-like staining of tumor cells and staining that accounted for more than 50% in the tissue sections were considered strong Myo9b staining and given a score of 3. Tissues with a score of 1 or lower were considered to have low Myo9b expression, whereas scores of 2 or higher were considered to have high Myo9b expression.

Microarray data analysis. The Oncomine database and gene microarray analysis tool (36), a repository for published cDNA microarray data, was explored for *SLIT2* mRNA expression in lung cancer and control samples. Oncomine algorithms were used to conduct statistical analyses of the differences in *SLIT2* expression. For patient survival analyses, the association between *SLIT2* or *MYO9B* expression and OS or PFS was assessed by Kaplan-Meier plotting, followed by log-rank testing for significance (37). cBioPortal software (www.cbioportal.org) was used to analyze gene mutation and gene expression correlations in 178 human lung cancer tissue samples (38).

Statistics. Comparisons were made using a 2-tailed Student's t test, a Mann-Whitney U test, or 1-way ANOVA. Pearson's χ^2 test was used to evaluate the relationship between Myo9b expression and clinicopathological features. Survival curves were calculated by the Kaplan-Meier method, and comparison was made using the log-rank test. A P value of less than 0.05 was considered statistically significant. All statistical calculations were performed using GraphPad Prism 5 (GraphPad Software) or SPSS 13.0 (IBM) software.

Study approval. All animal experiments were conducted according to institutional and national guidelines and following protocols approved by the IACUCs of the University of Chinese Academy of Sciences, the Chinese Academy of Sciences, and Northwestern University. All specimens were obtained with written informed consent of the patients in accordance with approved protocols and institutional and national guidelines.

Author contributions

JYW conceived the project idea, designed the studies, and supervised all aspects of the project. RK designed and carried out experiments and analyzed data. FY carried out experiments related to Myo9bGAP domain structural analyses. WF and LZ designed and supervised the structural analyses. JYW, XC, JL, LZ, and JR contributed to experiments and project coordination. PW, XL, YS, YN, KW, DF, and RK contributed to tissue sample collection and analyses. RK, FY, WF, LZ, and JYW wrote the manuscript.

Acknowledgments

We thank the team at the beamline BL17U of the Shanghai Synchrotron Radiation Facility for their help with x-ray crystallography. We also thank Xiang Du and Menghong Sun for their expert suggestions on immunohistochemical data analysis. We thank Jizhong Lou for the molecular dynamics simulations of the Myo9b RhoGAP/RhoA complex structure and Mang Zheng for technical assistance. We acknowledge members of the Wu laboratory for stimulating

discussions and suggestions. This work was supported by grants from the Ministry of Science and Technology of China (MOST) National Major Basic Research Program Projects (2011CB910503, 2013CB917803, and 2014CB910202); the National Natural Science Foundation of China (31190062, 31470746, 31300611, 31200577, 31200561, and 81225003); and the Chinese Academy of Science (CASN-GWPPS-2008). R. Kong was supported by a China Postdoctoral Science Foundation grant (20110490615). J.Y. Wu was supported by grants from the NIH (RO1CA175360 and RO1AG033004). We are grateful to the anonymous reviewers whose constructive critiques helped us improve our manuscript.

Address correspondence to: Li Zhu, State Key Laboratory of Brain and Cognitive Science, Institute of Biophysics, Chinese Academy of Sciences, Beijing, China. Phone: 86.10.6488.8303; E-mail: zhuli@moon.ibp.ac.cn. Or to: Wei Feng, National Laboratory of Biomacromolecules, Institute of Biophysics, Chinese Academy of Sciences, Beijing, China. Phone: 86.10.6488.8751; E-mail: wfeng@ibp.ac.cn. Or to: Jane Y. Wu, Department of Neurology, Center for Genetic Medicine, Lurie Cancer Center, Northwestern University Feinberg School of Medicine, 303 E. Superior St., Chicago, Illinois, USA. Phone: 312.503.0684; E-mail: jane-wu@northwestern.edu.

- Cooper WA, Lam DC, O'Toole SA, Minna JD. Molecular biology of lung cancer. *J Thorac Dis.* 2013;5(suppl 5):S479–S490.
- Peifer M, et al. Integrative genome analyses identify key somatic driver mutations of small-cell lung cancer. *Nat Genet.* 2012;44(10):1104–1110.
- Valastyan S, Weinberg RA. Tumor metastasis: molecular insights and evolving paradigms. *Cell.* 2011;147(2):275–292.
- Park KS, et al. A crucial requirement for Hedgehog signaling in small cell lung cancer. *Nat Med.* 2011;17(11):1504–1508.
- Brose K, et al. Slit proteins bind Robo receptors and have an evolutionarily conserved role in repulsive axon guidance. *Cell.* 1999;96(6):795–806.
- Li HS, et al. Vertebrate slit, a secreted ligand for the transmembrane protein roundabout, is a repellent for olfactory bulb axons. *Cell.* 1999;96(6):807–818.
- Wu W, et al. Directional guidance of neuronal migration in the olfactory system by the protein Slit. *Nature.* 1999;400(6742):331–336.
- Ypsilanti AR, Zagar Y, Chedotal A. Moving away from the midline: new developments for Slit and Robo. *Development.* 2010;137(12):1939–1952.
- Brantley-Sieders DM, et al. Angiocrine factors modulate tumor proliferation and motility through EphA2 repression of Slit2 tumor suppressor function in endothelium. *Cancer Res.* 2011;71(3):976–987.
- Geutskens SB, Hordijk PL, van Hennik PB. The chemorepellent Slit3 promotes monocyte migration. *J Immunol.* 2010;185(12):7691–7698.
- Legg JA, Herbert JM, Clissold P, Bicknell R. Slits and Roundabouts in cancer, tumour angiogenesis and endothelial cell migration. *Angiogenesis.* 2008;11(1):13–21.
- Prasad A, Qamri Z, Wu J, Ganju RK. Slit-2/Robo-1 modulates the CXCL12/CXCR4-induced chemotaxis of T cells. *J Leukoc Biol.* 2007;82(3):465–476.
- Wu JY, et al. The neuronal repellent Slit inhibits leukocyte chemotaxis induced by chemotactic factors. *Nature.* 2001;410(6831):948–952.
- Ballard MS, Hinck L. A roundabout way to cancer. *Adv Cancer Res.* 2012;114:187–235.
- Mehlen P, Delloye-Bourgeois C, Chedotal A. Novel roles for Slits and netrins: axon guidance cues as anticancer targets? *Nat Rev Cancer.* 2011;11(3):188–197.
- Nassarre P, Potiron V, Drabkin H, Roche J. Guidance molecules in lung cancer. *Cell Adh Migr.* 2010;4(1):130–145.
- Dammann R, et al. CpG island methylation and expression of tumour-associated genes in lung carcinoma. *Eur J Cancer.* 2005;41(8):1223–1236.
- Dallol A, et al. SLIT2, a human homologue of the Drosophila Slit2 gene, has tumor suppressor activity is frequently inactivated in lung breast cancers. *Cancer Res.* 2002;62(20):5874–5880.
- Kim HK, et al. Slit2 inhibits growth metastasis of fibrosarcoma squamous cell carcinoma. *Neoplasia.* 2008;10(12):1411–1420.
- Tseng RC, et al. SLIT2 attenuation during lung cancer progression deregulates β -catenin E-cadherin associates with poor prognosis. *Cancer Res.* 2010;70(2):543–551.
- Yu J, et al. The neuronal repellent SLIT2 is a target for repression by EZH2 in prostate cancer. *Oncogene.* 2010;29(39):5370–5380.
- Liao W, Elfrink K, Bahler M. Head of myosin IX binds calmodulin and moves processively toward the plus-end of actin filaments. *J Biol Chem.* 2010;285(32):24933–24942.
- van den Boom F, Dussmann H, Uhlenbrock K, Abouhamed M, Bahler M. The Myosin IXb motor activity targets the myosin IXb RhoGAP domain as cargo to sites of actin polymerization. *Mol Biol Cell.* 2007;18(4):1507–1518.
- Abouhamed M, et al. Myosin IXa regulates epithelial differentiation and its deficiency results in hydrocephalus. *Mol Biol Cell.* 2009;20(24):5074–5085.
- Hanley PJ, et al. Motorized RhoGAP myosin IXb (Myo9b) controls cell shape motility. *Proc Natl Acad Sci U S A.* 2010;107(27):12145–12150.
- Xu Y, et al. Dendritic cell motility and T cell activation requires regulation of Rho-cofilin signaling by the Rho-GTPase activating protein myosin IXb. *J Immunol.* 2014;192(8):3559–3568.
- Post PL, Bokoch GM, Mooseker MS. Human myosin-IXb is a mechanochemically active motor and a GAP for rho. *J Cell Sci.* 1998;111(pt 7):941–950.
- Saeki N, Tokuo H, Ikebe M. BIG1 is a binding partner of myosin IXb and regulates its Rho-GTPase activating protein activity. *J Biol Chem.* 2005;280(11):10128–10134.
- Wirth JA, Jensen KA, Post PL, Bement WM, Mooseker MS. Human myosin-IXb, an unconventional myosin with a chimerin-like rho/rac GTPase-activating protein domain in its tail. *J Cell Sci.* 1996;109(pt 3):653–661.
- Heasman SJ, Ridley AJ. Mammalian Rho GTPases: new insights into their functions from in vivo studies. *Nat Rev Mol Cell Biol.* 2008;9(9):690–701.
- Parsons JT, Horwitz AR, Schwartz MA. Cell adhesion: integrating cytoskeletal dynamics and cellular tension. *Nat Rev Mol Cell Biol.* 2010;11(9):633–643.
- Yuasa-Kawada J, Kinoshita-Kawada M, Rao Y, Wu JY. Deubiquitinating enzyme USP33/VDU1 is required for Slit signaling in inhibiting breast cancer cell migration. *Proc Natl Acad Sci U S A.* 2009;106(34):14530–14535.
- Wong K, et al. Signal transduction in neuronal migration: roles of GTPase activating proteins and the small GTPase Cdc42 in the Slit-Robo pathway. *Cell.* 2001;107(2):209–221.
- Jaffe AB, Hall A. Rho GTPases: biochemistry and biology. *Annu Rev Cell Dev Biol.* 2005;21:247–269.
- Yuasa-Kawada J, Kinoshita-Kawada M, Wu G, Rao Y, Wu JY. Midline crossing and Slit responsiveness of commissural axons require USP33. *Nat Neurosci.* 2009;12(9):1087–1089.
- Rhodes DR, et al. ONCOMINE: a cancer microarray database and integrated data-mining platform. *Neoplasia.* 2004;6(1):1–6.
- Gyorffy B, Surowiak P, Budczies J, Lanczky A. Online survival analysis software to assess the prognostic value of biomarkers using transcriptomic data in non-small-cell lung cancer. *PLoS One.* 2013;8(12):e82241.
- Gao J, et al. Integrative analysis of complex cancer genomics and clinical profiles using the cBioPortal. *Sci Signal.* 2013;6(269):p1.
- Spiro SG, Silvestri GA. One hundred years of lung cancer. *Am J Respir Crit Care Med.* 2005;172(5):523–529.
- Sanchez-Cespedes M. The role of LKB1 in lung cancer. *Fam Cancer.* 2011;10(3):447–453.
- Vahtomeri K, Makela TP. Molecular mechanisms of tumor suppression by LKB1. *FEBS Lett.* 2011;585(7):944–951.
- Yiin JJ, et al. Slit2 inhibits glioma cell invasion in the brain by suppression of Cdc42 activity. *Neuro Oncol.* 2009;11(6):779–789.
- Werbowski-Ogilvie TE, et al. Inhibition of medulloblastoma cell invasion by Slit. *Oncogene.* 2006;25(37):5103–5112.
- Greenberg JM, Thompson FY, Brooks SK, Shannon JM, Akeson AL. Slit and robo expression in the developing mouse lung. *Dev Dyn.* 2004;230(2):350–360.
- Muller RT, Honnert U, Reinhard J, Bahler M. The rat myosin myr 5 is a GTPase-activating protein for Rho in vivo: essential role of arginine 1695. *Mol Biol Cell.* 1997;8(10):2039–2053.
- Jelen F, Lachowicz P, Apostoluk W, Mateja A, Derewenda ZS, Otlewski J. Dissecting the thermodynamics of GAP-RhoA interactions. *J Struct Biol.* 2009;165(1):10–18.
- Ridley AJ. Life at the leading edge. *Cell.* 2011;145(7):1012–1022.

48. Besson A, Gurian-West M, Schmidt A, Hall A, Roberts JM. p27Kip1 modulates cell migration through the regulation of RhoA activation. *Genes Dev.* 2004;18(8):862–876.
49. Kurokawa K, Matsuda M. Localized RhoA activation as a requirement for the induction of membrane ruffling. *Mol Biol Cell.* 2005;16(9):4294–4303.
50. Wu X, Liu T, Fang O, Leach LJ, Hu X, Luo Z. miR-194 suppresses metastasis of non-small cell lung cancer through regulating expression of BMP1 p27(kip1). *Oncogene.* 2014;33(12):1506–1514.
51. Liu Y, et al. Ablation of p120-catenin enhances invasion and metastasis of human lung cancer cells. *Cancer Sci.* 2009;100(3):441–448.
52. Cools J. RHOA mutations in peripheral T cell lymphoma. *Nat Genet.* 2014;46(4):320–321.
53. Kakiuchi M, et al. Recurrent gain-of-function mutations of RHOA in diffuse-type gastric carcinoma. *Nat Genet.* 2014;46(6):583–587.
54. Palomero T, et al. Recurrent mutations in epigenetic regulators, RHOA and FYN kinase in peripheral T cell lymphomas. *Nat Genet.* 2014;46(2):166–170.
55. Sakata-Yanagimoto M, et al. Somatic RHOA mutation in angioimmunoblastic T cell lymphoma. *Nat Genet.* 2014;46(2):171–175.
56. Wang K, et al. Whole-genome sequencing and comprehensive molecular profiling identify new driver mutations in gastric cancer. *Nat Genet.* 2014;46(6):573–582.
57. Yoo HY, et al. A recurrent inactivating mutation in RHOA GTPase in angioimmunoblastic T cell lymphoma. *Nat Genet.* 2014;46(4):371–375.
58. Zhou J, Hayakawa Y, Wang TC, Bass AJ. RhoA mutations identified in diffuse gastric cancer. *Cancer Cell.* 2014;26(1):9–11.
59. Battye TG, Kontogiannis L, Johnson O, Powell HR, Leslie AG. iMOSFLM: a new graphical interface for diffraction-image processing with MOSFLM. *Acta Crystallogr D Biol Crystallogr.* 2011;67(pt 4):271–281.
60. Dodson EJ, Winn M, Ralph A. Collaborative Computational Project, number 4: providing programs for protein crystallography. *Methods Enzymol.* 1997;277:620–633.
61. McCoy AJ. Solving structures of protein complexes by molecular replacement with Phaser. *Acta Crystallogr D Biol Crystallogr.* 2007;63(pt 1):32–41.
62. Emsley P, Cowtan K. Coot: model-building tools for molecular graphics. *Acta Crystallogr D Biol Crystallogr.* 2004;60(pt 12 pt 1):2126–2132.
63. Adams PD, et al. PHENIX: a comprehensive Python-based system for macromolecular structure solution. *Acta Crystallogr D Biol Crystallogr.* 2010;66(pt 2):213–221.
64. Laskowski RA, Macarthur MW, Moss DS, Thornton JM. Procheck — a program to check the stereochemical quality of protein structures. *J Appl Cryst.* 1993;26(2):283–291.
65. Phillips JC, et al. Scalable molecular dynamics with NAMD. *J Comput Chem.* 2005;26(16):1781–1802.
66. MacKerell AD, et al. All-atom empirical potential for molecular modeling and dynamics studies of proteins. *J Phys Chem B.* 1998;102(18):3586–3616.
67. Humphrey W, Dalke A, Schulten K. VMD: visual molecular dynamics. *J Mol Graph.* 1996;14(1):33–38.
68. Tong X, et al. Decreased TIP30 expression promotes tumor metastasis in lung cancer. *Am J Pathol.* 2009;174(5):1931–1939.